The Astrophysical Journal, 707:343–353, 2009 December 10 doi:10.1088/0004-637X/707/1/343

THE EFFECT OF ASYMMETRIC BEAMS IN THE *WILKINSON MICROWAVE ANISOTROPY PROBE* EXPERIMENT

I. K. Wehus[1], L. Ackerman[2], H. K. Eriksen[3,4], and N. E. Groeneboom[3,4]
[1] Department of Physics, University of Oslo, P.O. Box 1048, Blindern, N-0316 Oslo, Norway; i.k.wehus@fys.uio.no
[2] California Institute of Technology, Pasadena, CA 91125, USA; lotty@caltech.edu
[3] Institute of Theoretical Astrophysics, University of Oslo, P.O. Box 1029, Blindern, N-0315 Oslo, Norway; h.k.k.eriksen@astro.uio.no
[4] Centre of Mathematics for Applications, University of Oslo, P.O. Box 1053, Blindern, N-0316 Oslo, Norway; leuat@irio.co.uk
Received 2009 April 25; accepted 2009 October 21; published 2009 November 20

ABSTRACT

We generate simulations of the cosmic microwave background (CMB) temperature field as observed by the *Wilkinson Microwave Anisotropy Probe* (*WMAP*) satellite, taking into account the detailed shape of the asymmetric beams and scanning strategy of the experiment, and use these to re-estimate the *WMAP* beam transfer functions. This method avoids the need of artificially symmetrizing the beams, as done in the baseline *WMAP* approach, and instead measures the total convolution effect by direct simulation. We find only small differences with respect to the nominal transfer functions, typically less than 1% everywhere, and less than 0.5% at $\ell < 400$. The net effect on the CMB power spectrum is less than 0.6%. The effect on all considered cosmological parameters is negligible. For instance, we find that the spectral index of scalar perturbations after taking into account the beam asymmetries is $n_s = 0.964 \pm 0.014$, corresponding to a negative shift of -0.1σ compared to the previously released *WMAP* results. Our CMB sky simulations are made publicly available and can be used for general studies of asymmetric beam effects in the *WMAP* data.

Key words: cosmic microwave background – cosmology: observations – methods: statistical

Online-only material: color figures

1. INTRODUCTION

Without a doubt, the angular cosmic microwave background (CMB) power spectrum is today our single most important source of cosmological information. Perhaps the most striking demonstration of this fact to date is the *Wilkinson Microwave Anisotropy Probe* (*WMAP*) experiment (Bennett et al. 2003; Hinshaw et al. 2007, 2009), which has allowed cosmologists to put unprecedented constraints on all main cosmological parameters, as well as ruling out vast regions of the possible model spaces. Similarly, in only a few years from now *Planck* will finally provide the definitive measurements of the temperature power spectrum, as well as polarization spectra with unprecedented accuracy. This will certainly lead to similar advances in our knowledge about the history of our universe.

Each of these experiments observes the CMB field by scanning the sky with an instrumental beam of finite resolution. This operation effectively corresponds to averaging over beam-sized angular scales and is expressed technically either in pixel space by a convolution of the beam with the underlying sky, or in harmonic space by a multiplication of the two corresponding sets of harmonic expansion coefficients. For simplicity, the harmonic space expansion of the beam is typically expressed in terms of Legendre coefficients of an (azimuthally symmetric) effective beam response. This function is often called the "beam transfer function," b_ℓ.

Before it is possible to make unbiased cosmological inferences based on the CMB power spectrum, it is of critical importance to know the beam transfer function to high precision, as an error in the beam function translates into a direct bias in the estimated power spectrum. This in turn requires detailed knowledge about the beam response function on the sky for each experiment. For a full description of the *WMAP* beam estimation process and final model, see Page et al. (2003), Jarosik et al. (2007), and Hill et al. (2009).

The impact of asymmetric beams may also be important for applications other than power spectrum estimation. One example of special interest to us is the assessment of non-Gaussianity and violation of statistical isotropy. Specifically, Ackerman et al. (2007) considered a model based on violation of rotational invariance in the early universe and derived explicit parametric expressions for the corresponding observational signature. Then, in a follow-up paper, Groeneboom & Eriksen (2009) analyzed the 5-year *WMAP* data with respect to this model and, most surprisingly, found a detection at the 3.8σ confidence level. Given that this was a most unexpected result, several questions concerning systematic errors in the *WMAP* data were considered, in particular those due to residual foregrounds, correlated noise, and asymmetric beams. However, it was shown in the same paper that neither foregrounds nor correlated noise were viable explanations, while the question of asymmetric beams was left unanswered due to lack of proper simulation machinery. This question provided our initial motivation for considering the problems studied in this paper.

The starting point for tackling the asymmetric beam problem for *WMAP* is a set of beam maps released by the *WMAP* team, two for each differencing assembly (DA), denoted by A and B, respectively. These maps were derived by observing Jupiter for extended periods of time. Then, in order to derive the proper beam transfer functions, the *WMAP* team adopted a computationally fast and convenient approach: they first symmetrized the effective beam for each DA, collapsing the information in the A and B sides into one common function, and then computed the Legendre transform of the corresponding radial profile. However, for this to be an accurate approximation, one must on the one hand assume that the beams on the two sides are very similar, and on the other hand, assume either that both beams are intrinsically circularly symmetric, or that all pixels on the sky are observed from all angles an equal number of times due to the scanning strategy. In reality none of these conditions

are met, and one may therefore ask whether there might be any residual effect due to the combination of an asymmetric beam and anisotropic scanning in the *WMAP* beam functions.

This problem was addressed analytically by Hinshaw et al. (2007), who derived an approximate expression for the expected power spectrum bias due to asymmetric beams in the *WMAP* data. Their conclusion was that such effects were $\lesssim 1\%$ for the 3-year *WMAP* data.

In this paper, we revisit the question of asymmetric beams in *WMAP* with two main goals. First, we seek to estimate the effective beam transfer functions for each *WMAP* DA, taking into account the full details of the asymmetric beams and specifics of the *WMAP* scanning strategy by direct simulation. This way, we check whether the analytic approximations presented by Hinshaw et al. (2007) are valid. Second, we want to produce a set of high-fidelity simulated CMB sky maps, with beam properties as close as possible to those observed by *WMAP*, that can later be used for general studies of asymmetric beam effects in *WMAP*.

2. PIPELINE OVERVIEW

In this section, we summarize the methods and algorithms used in this paper. Note that none of the individual steps described below are original to this paper and only the main ideas will therefore be discussed in the following.

We begin by defining our notation. We will be estimating the product of the *WMAP* beam transfer function, b_ℓ, and pixel window, p_ℓ, by direct simulation. This product is denoted by $\beta_\ell = b_\ell p_\ell$. Given this function, the combined effect on a sky map, $T(\hat{n})$, of convolution by an instrumental beam and averaging over finite-sized pixels may be approximated in harmonic space as

$$T(\hat{n}) = \sum_{\ell=0}^{\ell_{\rm max}} \sum_{m=-\ell}^{\ell} \beta_\ell a_{\ell m} Y_{\ell m}(\hat{n}), \quad (1)$$

where $Y_{\ell m}(\hat{n})$ are the usual spherical harmonics.

The angular power spectrum of T is given by

$$\hat{C}_\ell = \frac{1}{2\ell+1} \sum_{m=-\ell}^{\ell} \beta_\ell^2 |a_{\ell m}|^2, \quad (2)$$

while the power spectrum of the true underlying CMB map, $s(\hat{n})$, is

$$C_\ell = \frac{1}{2\ell+1} \sum_{m=-\ell}^{\ell} |a_{\ell m}|^2. \quad (3)$$

The effect of the beam convolution and pixel averaging on the power spectrum is therefore simply given by a multiplication with β_ℓ^2.

The overall approach for estimating β_ℓ used in this paper may be summarized by the following steps: first, we simulate time-ordered data (TOD) for each DA, taking into account both the detailed beam maps of *WMAP* and the exact orientation of the spacecraft at each point in time. We then produce a sky map from this TOD. Next we compute the square root of the ratio between the output and the input power spectra. Finally, because the input beam maps themselves are pixelized, and therefore slightly smoothed, we also have to divide out (or deconvolve) the pixel window of the beam pixelization. The resulting function becomes our estimate of the beam transfer function, β_ℓ.

Note that in this paper we are only concerned with the effect of asymmetric beams, not other systematic effects such as instrumental noise. All following discussions will therefore assume noiseless observations.

2.1. Simulation of Time-ordered Data

Our first step is to simulate a reference CMB sky realization, s, given an angular temperature power spectrum, $C_\ell^{\rm theory}$. This can be achieved with a standard code such as "anafast," which is available in the HEALPix[5] software package. Note that this map should not be smoothed with either an instrumental beam or a pixel window; adding these effects is the task of the following pipeline. Explicitly, the input reference map should simply be pure spherical harmonic modes projected onto a set of pixel centers.

Next, we need to be able to convolve this map with a given beam map at arbitrary positions and orientations on the sphere. In this paper, we do this by brute-force integration in pixel space. For an alternative fast Fourier space-based approach to the same problem, see Wandelt & Górski (2001).

We define $\hat{p}$ to be a unit vector pointing toward the beam center and specify its position on the sphere using longitude and co-latitude (ϕ, θ). We further define ψ to be the angle between some fixed reference direction in the beam map and the local meridian. The value of the beam map at position $\hat{n} = (\phi', \theta')$, which in principle is non-zero over the full sky, is denoted $b(\phi', \theta'; \phi, \theta, \psi)$. With these definitions, the desired convolution may be written as

$$T(\phi, \theta, \psi) = \int_{4\pi} s(\phi', \theta') b(\phi', \theta'; \phi, \theta, \psi) d\Omega'. \quad (4)$$

Computationally speaking, we approximate this integral as a direct sum over HEALPix pixels, which all have equal area, with the product $s \cdot b$ being evaluated at HEALPix pixel centers. To make these calculations computationally feasible, we assume that the beam is zero beyond some distance from the beam center (ranging between $3\overset{\circ}{.}5$ and 7° for the *WMAP* channels), and thus only include the main lobe in the following analysis. While the *WMAP* beam maps are provided as pixelized maps, we need to know the beam values at arbitrary positions (i.e., HEALPix pixel centers). We solve this by computing a two-dimensional spline for each beam map, enabling us to interpolate to arbitrary positions. For a review on one specific method for fast (and local) two-dimensional spline evaluations, see Appendix B.

WMAP is a differential experiment and measures at each point of time the difference between the signals received by two different detectors, denoted by A and B. The full set of time-ordered *WMAP* data may therefore be written as

$$d_x(i) = T_x^{\rm A}(i) - T_x^{\rm B}(i), \quad (5)$$

where $x = \{{\rm K1}, {\rm Ka1}, {\rm Q1-2}, {\rm V1-2}, {\rm W1-4}\}$ is a DA label, and i is a time index and for each detector a shorthand for (ϕ, θ, ψ). This equation may be written in the following matrix form:

$$\mathbf{d}_x = \mathbf{A}\mathbf{T}_x \quad (6)$$

where we have introduced an $N_{\rm tod} \times N_{\rm pix}$ pointing matrix $\mathbf{A}$. This matrix contains two numbers per row; 1 in the column hit by the center of beam A at time i, and -1 in the column hit by the center of beam B.

The remaining problem is to determine the position and orientation of each detector at each time step. This information

[5] http://healpix.jpl.nasa.gov

has been made publicly available by the *WMAP* team on the Legacy Archive for Microwave Background Data Analysis (LAMBDA),[6] and consists of a large set of pointing files together with useful routines for extracting the desired information.

2.2. Map Making with Differential Data

For the map making step we adopt the algorithm developed by Wright et al. (1996), which was used in the 1-year *WMAP* pipelines (Hinshaw et al. 2003). Here we only summarize the essential algebra and outline the algorithm.

Our goal is to establish an unbiased and, preferably, optimal estimate of the (smoothed) sky signal, $\hat{\mathbf{T}}$, given a set of differential TOD values, $\mathbf{d}$. For noiseless data, the maximum likelihood estimator is simply

$$\hat{\mathbf{T}} = (\mathbf{A}^t\mathbf{A})^{-1}\mathbf{A}^t\mathbf{d}. \tag{7}$$

For high-resolution sky maps, this equation involves an inverse of a large matrix and cannot be solved explicitly. Instead, one often resorts to iterative methods such as conjugate gradients, or, for differential data, the method developed by Wright et al. (1996).

We present the iterative differential map maker in a simple manner: define $\mathbf{D}$ to be the diagonal matrix that counts the number of hits $N_{\rm obs}(p)$ per pixel p on the diagonal, and a_i and b_i to be the pixels hit by sides A and B at time i, respectively. Suppose that we already have established some estimate for the solution, $\hat{\mathbf{T}}^j$ (note that this can be zero). Then the iterative scheme

$$\hat{\mathbf{T}}^{j+1} = \hat{\mathbf{T}}^j + \mathbf{D}^{-1}\mathbf{A}^t(\mathbf{d} - \mathbf{A}\hat{\mathbf{T}}^j) \tag{8}$$

will converge to the true solution: if $\hat{\mathbf{T}}^j = \mathbf{T}$, then $\mathbf{d} = \mathbf{A}\hat{\mathbf{T}}^j$, and the second term on the right-hand side is zero. This algorithm is implemented by the following scheme:

$$\hat{T}_p^{j+1} = \frac{\sum_i \left(\delta_{p,a_i}\left[\hat{T}_{b_i}^j + d_i\right] + \delta_{p,b_i}\left[\hat{T}_{a_i}^j - d_i\right]\right)}{N_{\rm obs}(p)}. \tag{9}$$

This algorithm was originally presented by Wright et al. (1996). The only new feature introduced here is the choice of the starting point. In the original paper, Wright et al. (1996) initialized the iterations at the Differential Microwave Radiometer dipole, since their test simulation included a CMB dipole term. However, for a given scanning strategy, there will often be some large-scale modes that are less well sampled than others. For instance, for the *WMAP* strategy, $\ell = 5$ is more problematic than other modes (Hinshaw et al. 2003). This leads to slow convergence with the above scheme for this mode.

We therefore choose a different approach: before solving for the high-resolution map by iterations, we solve Equation (7) by brute-force at low resolution. For the cases considered later in this paper, we choose a HEALPix resolution of $N_{\rm side} = 16$ for this purpose. With 3072 pixels, about 30 s are needed to solve this system by singular value decomposition. (Note that the monopole is arbitrary for differential measurements, and one must therefore use an eigenvalue decomposition type algorithm to solve the system.) The improvement in convergence speed due to this choice of initial guess is explicitly demonstrated in Appendix A.

Our convergence criterion is chosen such that the rms difference between two consecutive iterations must be less than 0.05 μK. We have verified that this leads to errors of less than 0.1 μK in the final solution, of which most is due to a residual dipole. This is typically achieved with 30–50 iterations, although some converge already after 20–30 iterations and a few after 70 or more iterations.

At first glance, the fact that the final residuals are as small as 0.1 μK for an rms stopping criterion as large as 0.05 μK may seem surprising. However, this is explained by the fact that the iterative solution obtained by Equation (8) often alternates between high and low values about the true answer. This suggests that a further improvement to the algorithm may be possible: faster convergence may perhaps be obtained by computing the average of two consecutive iterations, $\hat{\mathbf{T}} = (\hat{\mathbf{T}}^j + \hat{\mathbf{T}}^{j+1})/2$, as the map estimate for iteration $j+2$. However, the computational resources spent during map making is by far sub-dominant compared to the TOD simulation, and we have therefore not yet implemented this step in our codes.

2.3. Estimation of Hybrid Beam Transfer Functions

As described in the introduction to this section, we estimate the transfer function by the square root of the ratio between the power spectra of the convolved map and the input map

$$\hat{\beta}_\ell^2 = \sqrt{\frac{\hat{C}_\ell}{C_\ell}}. \tag{10}$$

However, as noted above, this function describes both the effect from instrumental beam smoothing and averaging over pixels. In the present paper, we are concerned mostly with the former of these two effects, which has a stronger impact on large to intermediate scales.

In the following, we choose to construct a hybrid transfer function

$$\hat{\beta}_\ell = \begin{cases} \sqrt{\frac{\hat{C}_\ell}{C_\ell}} & \text{for} \quad \ell \leqslant \ell_{\rm hybrid} \\ \sqrt{\frac{\hat{C}_{\ell_{\rm hybrid}}}{C_{\ell_{\rm hybrid}}}} \frac{b_\ell^{WMAP}}{b_{\ell_{\rm hybrid}}^{WMAP}} \frac{p_\ell}{p_{\ell_{\rm hybrid}}} & \text{for} \quad \ell > \ell_{\rm hybrid} \end{cases}. \tag{11}$$

Here b_ℓ^{WMAP} is the nominal symmetrized transfer function published by the *WMAP* team, p_ℓ is the (uniformly averaged) HEALPix pixel window, and $\ell_{\rm hybrid}$ is some transition multipole. In other words, we adopt our own direct estimate of the transfer function up to $\ell_{\rm hybrid}$, but adopt the symmetrized, asymptotically uniform, and properly scaled *WMAP* transfer function at higher multipoles.

Note that this issue is of minor importance in terms of cosmological interpretation, i.e., angular power spectrum and cosmological parameters, because the transition typically takes place in the noise dominated high-ℓ regime. The effect of the anisotropic pixel window is therefore largely suppressed. In the present paper, we therefore choose to focus on the beam dominated region and leave a detailed study of the pixel window to a future paper.

Finally, because we only generate a relatively small number of simulations in this paper, there is considerable Monte Carlo scatter in our estimated transfer functions on an ℓ-by-ℓ basis. To reduce this Monte Carlo noise, we smooth all transfer functions using the smooth spline formalism described by, e.g., Green & Silverman (1994).

[6] http://lambda.gsfc.nasa.gov

Table 1
Summary of DA Parameters

DA	FWHM[a] (arcmin)	Radius[b] (deg)	$N_{\rm side}$	$\ell_{\rm max}$	$\ell_{\rm hybrid}$	$N_{\rm samples}$ (10^8)	$\sigma_{\rm N}$[c] (μK)
K1	53	7.0	512	750	318	2.5	...
Ka1	40	5.5	512	850	411	2.5	...
Q1	31	5.0	512	1100	522	3.1	78.2
Q2	31	5.0	512	1100	515	3.1	74.2
V1	21	4.0	1024	1500	789	4.1	99.0
V2	21	4.0	1024	1500	779	4.1	88.2
W1	13	3.5	1024	1700	1164	6.2	143.8
W2	13	3.5	1024	1700	1148	6.2	159.7
W3	13	3.5	1024	1700	1162	6.2	168.5
W4	13	3.5	1024	1700	1169	6.2	164.4

Notes.
[a] Effective symmetrized beam size.
[b] Radius used for pixelized beam convolutions. See Hill et al. (2009) for details.
[c] Average full-sky rms values evaluated at $N_{\rm side} = 512$.

3. DATA AND SIMULATIONS

All data products used in this study are provided by the *WMAP* team on LAMBDA as part of their 5-year data release. However, the calculations performed here are computationally extremely demanding, and we therefore include only roughly 1 year worth of data in our calculations. To be precise, we include the period between 2001 July 10 and 2002 August 2, except for 3 days with missing data, for a total of 383 days.[7]

We consider all 10 *WMAP* DAs in our calculations, which are denoted, in order from low to high frequencies, K1 (23 GHz), Ka1 (33 GHz), Q1–2 (41 GHz), V1–2 (61 GHz), and W1–4 (94 GHz), respectively. Their resolutions range from 53′ FWHM at *K* band to 13′ FWHM at *W* band. Because of this large range in resolution, we specify the pixel resolution and harmonic space range for each case separately. For instance, *K* band is pixelized at $N_{\rm side} = 512$ and includes multipoles up to $\ell_{\rm max} = 750$ (the highest multipole present in the transfer function provided by the *WMAP* team), while the *W* band is pixelized at $N_{\rm side} = 1024$ and includes multipoles up to $\ell_{\rm max} = 1700$. A full summary of all relevant parameters for each DA is given in Table 1.

Note that the listed noise rms values are only used for estimating the power spectrum weights in Section 6. For simplicity we have adopted the official rms values for the foreground-reduced 5-year *WMAP* maps here, but note that there is a ∼1% bias in some of these values (Groeneboom et al. 2009). However, this has no significant impact on the results presented in this paper.

The beam maps for each DA are provided in the form of pixelized maps, and separately for side A and B. Each beam map contains non-zero values inside a radius around the beam center which is specified for each DA. For instance, the *K*-band radius is 7°, and the *W*-band radius is 3°.5. When evaluating the convolution defined in Equation (4), we include all pixels inside this radius.

The pixel size of the beam maps is 2′.4, which oversamples even the *W*-band beams. Based on these high-resolution maps we precompute all coefficients of the corresponding bi-cubic spline (see Appendix B), which allows us to very quickly interpolate at arbitrary positions in the beam map with high accuracy.

The pixel window of the 2′.4 beam pixelization is also provided on LAMBDA, and is taken into account by deconvolving final results wherever appropriate. Note that this effect must also be taken properly into account by other users who wish to use our simulations for follow-up studies.

Each beam is normalized by convolving a map constant equal to 1 at 1000 random positions and orientations, and demanding that the average of the resulting 1000 values equals unity. With the two-dimensional spline interpolation scheme described in Appendix B the random uncertainties on the normalization due to beam position and orientation are ∼0.2%. For comparison, directly reading off pixel values from the beam maps without interpolation leads to variations in the normalization at the ∼2% level.

For our base CMB reference sky set, we draw ten random Gaussian realizations from the best-fit ΛCDM power spectrum derived from the 5-year *WMAP* data alone (Komatsu et al. 2009). These maps are generated at both ($N_{\rm side} = 512$ and $N_{\rm side} = 1024$) using the same seeds, and include neither an instrumental beam nor a pixel window; they are simply spherical harmonic modes projected onto the HEALPix pixel centers. All ten realizations are processed for all ten DAs, such that the resulting simulations may be used for multifrequency analysis, if so desired.

As noted above, the computational requirements for the analyses presented here are demanding. The CPU time for processing a single *W*-band DA is ∼4000 hr, and the total disk usage for the entire project is ∼1 TB. For comparison, the corresponding map making step requires ∼60 CPU hr, and is thus completely sub-dominant to the TOD simulation.

4. COMPARISON WITH ANALYTIC CASE

In order to test our pipeline and understand its outputs, we start by considering a perfect Gaussian beam. This case is treated in two different ways: first, we convolve a CMB realization directly in harmonic space (as defined by Equation (1)) with a $\sigma_{\rm FWHM} = 20'$ FWHM analytic Gaussian beam and the appropriate HEALPix pixel window, p_ℓ, for $N_{\rm side} = 1024$. The combined transfer function for this case reads

$$\beta_\ell^{\rm ref} = e^{-\frac{1}{2}\ell(\ell+1)\sigma^2} p_\ell, \tag{12}$$

where $\sigma = \sigma_{\rm fwhm}/\sqrt{8\ln 2}$ and $\sigma_{\rm fwhm}$ is expressed in radians.

Second, we map out a corresponding two-dimensional Gaussian in pixel space over a grid of 2′.4 pixels, the same resolution as the *WMAP* beam maps. We then input this into our simulation pipeline together with the same CMB realization used for the analytic convolution, and with the V1 channel pointing sequence. From the resulting brute-force convolved map, we then obtain the effective transfer function, β_ℓ, as described in Section 2.3.

This function is plotted in the top panel of Figure 1, together with the product of the analytic Gaussian beam and the HEALPix pixel window. The ratio of the two effective functions is shown in the lower panel.

From this figure, it is clear that the agreement between the two approaches is excellent up to $\ell \approx 800$. At higher ℓ's, however, the ratio increases rapidly, indicating that the analytic approach smooths more than the brute-force approach.

In practice, one is well advised not to consider scales smaller than those that are properly oversampled by the scanning strategy. In this paper, we adopt the analytic case considered in this

[7] Our original intention was to include precisely 1 year of observations in our analysis, and therefore we processed 365 *WMAP* pointing files. However, we noticed after the calculations were completed that some of the pointing files contained slightly more than 1 day's worth of data, such that a total of 383 days were in fact included.

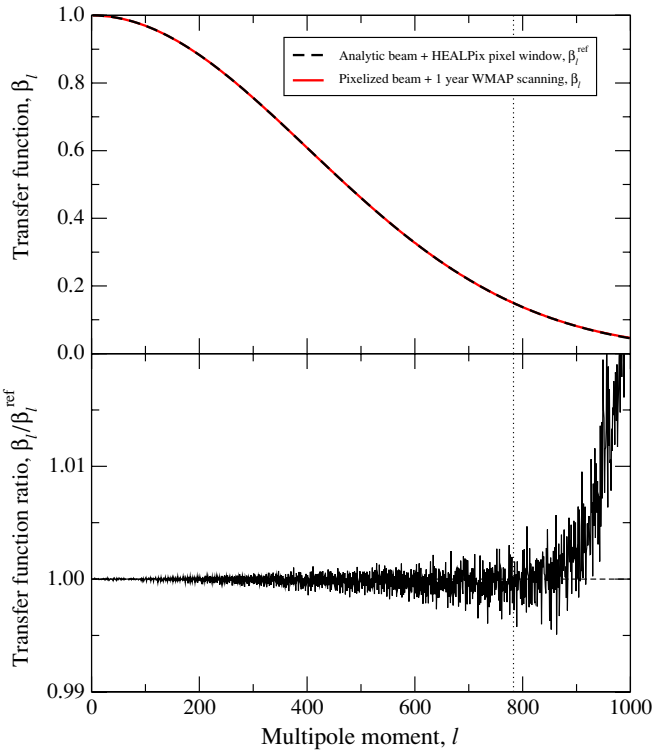

Figure 1. Top panel: comparison between the transfer functions, β_ℓ, for a Gaussian beam of 20′ FWHM. This was computed from a pixelized beam map and with the *WMAP* V1 scanning strategy (red line), and alternatively, by using the well-known analytic expression for the Legendre transform of a Gaussian beam (Equation (12)) and isotropized HEALPix pixel window (black dashed line). The vertical dotted line indicates the multipole moment, $\ell_{\rm hybrid}$, at which $\beta_\ell = 0.15$. Bottom panel: ratio between the transfer functions in the top panel. Note the excellent agreement up to $\ell \approx 800$, after which the differences in pixel window approximations becomes visible.

(A color version of this figure is available in the online journal.)

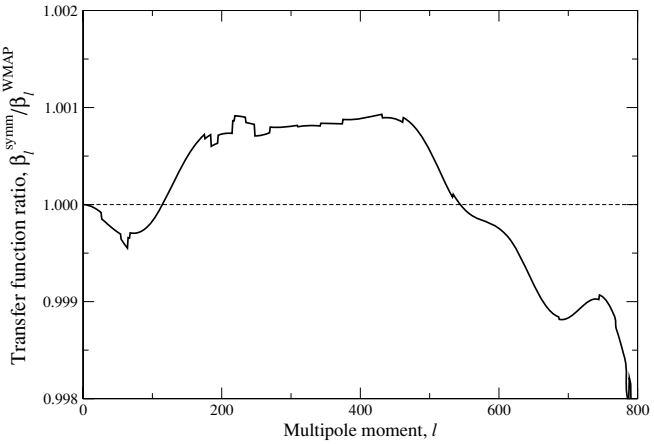

Figure 2. Comparison of the beam transfer functions derived from our symmetrized beam profile of the V1 DA with the official *WMAP* beam transfer function. The differences between the two symmetrized transfer functions are generally smaller than 0.1%, indicating that the inputs to our analysis are consistent with the *WMAP* inputs.

section to guide us in determining which scale that is. Explicitly, we conservatively demand that the effective beam transfer function must be greater than 0.15 in order to consider it to be properly oversampled, and therefore independent of scanning strategy. We adopt the corresponding multipole moment to be $\ell_{\rm hybrid}$, as defined in Section 2.3. Thus, the symmetrized *WMAP* beam and HEALPix pixel window are used at scales for which the beam amplitude drops below 0.15.

This test shows that the computational machinery described in Section 2 works as expected. However, it does not validate the inputs. Therefore, to check that our input data are consistent with those used in the official *WMAP* analysis (Page et al. 2003; Jarosik et al. 2007; Hill et al. 2009), we repeat their approach of Legendre transforming a symmetrized beam profile, $b_{\rm s}(\theta)$, into the harmonic space transfer function, b_ℓ, but now derive $b_{\rm s}(\theta)$ from our two-dimensional beam splines.

The result from one of these computations is shown in Figure 2. Here we see that the agreement is better than 0.1% over most of the range.

5. THE EFFECT OF ASYMMETRIC BEAMS IN *WMAP*

We now present the main results obtained in this paper, namely the effective beam transfer functions for each *WMAP* DA, taking into account both the full asymmetric beam patterns and scanning strategy. These are shown in Figure 3 (red lines) and compared to the nominal *WMAP* transfer functions (dashed black lines). The vertical dotted line indicates $\ell_{\rm hybrid}$ for each case.

Clearly, the differences between the two sets of results are small, as no visual discrepancies are seen in this plot. In Figure 4, we plot the ratio between our transfer functions and the *WMAP* transfer functions for $\ell \leqslant \ell_{\rm hybrid}$, and now we do see small but significant differences between the two sets of results.

Before looking at the results, we note that the completely symmetrized transfer function constitutes a lower bound on the full transfer function: when symmetrizing the beam, any beam mode with $m \neq 0$ is nullified. Consequently, less power is retained after convolution with the symmetrized beam than when an arbitrary beam is considered.

In Figure 4 we see precisely this behavior. Explicitly, we see that the ratios are essentially unity on the largest scales (smallest ℓ's), and then increase with higher ℓ's. (Some functions show values slightly lower than unity over short ranges, typically $\lesssim$0.2%, and this is due to small differences in the two beam models used by *WMAP* and our analysis; similar differences are observed when comparing symmetrized transfer functions. See Figure 2.)

The point at which the two transfer functions start to diverge varies somewhat from DA to DA, and depends of course on the angular scale of the particular DA. For instance, W2 and W3 start to diverge already at $\ell \sim 200$, while W1 and W4 are very close up to $\ell \sim 800$. On the other hand, all the low-frequency DAs are generally close to unity up to $\ell \sim 200$–300.

These general and qualitative remarks reflect the position of each DA in the *WMAP* focal plane (see Figure 6 of Jarosik et al. 2007 for an excellent visualization of the A side beams): K1, Ka1, and Q1–2 are positioned the furthest away from the optical axis, while V1–2 and W1–4 are the closest. Similarly, W1 and W4 are positioned lower in elevation, and generally have more sub-structure, than W2 and W3.

However, it should be emphasized that the overall differences are small, typically less than 1% at $\ell \leqslant \ell_{\rm hybrid}$. Further, these differences are only significant (again, with the exception of W1 and W4) in the intermediate- and high-ℓ ranges.

To build up some intuitive understanding of the spatial variations caused by the asymmetric *WMAP* beams, we show in Figure 5 the difference between the fully asymmetrically convolved map and the corresponding map convolved with the

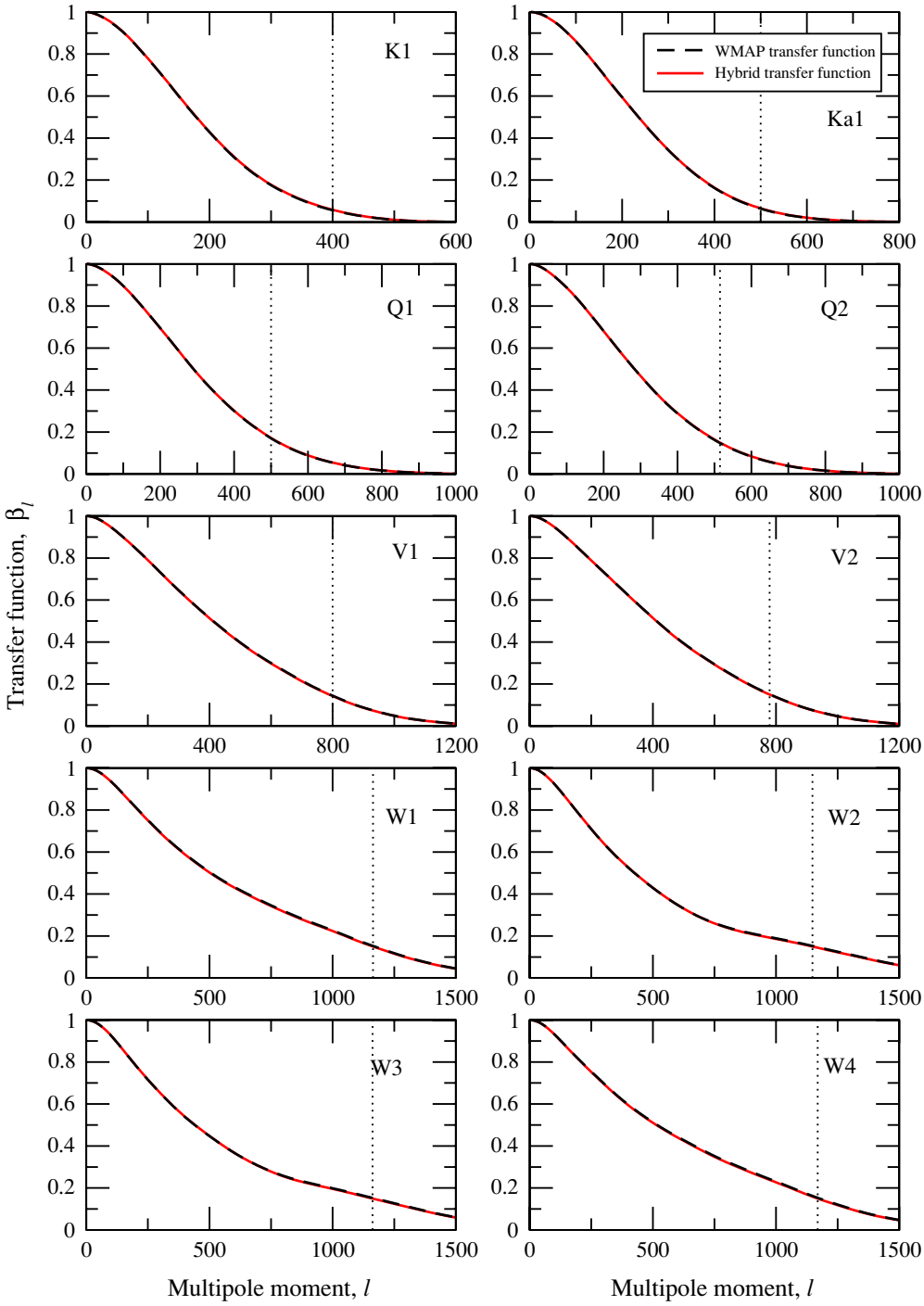

Figure 3. Comparison between transfer functions derived in this paper (red lines) and the nominal *WMAP* transfer functions (black dashed lines). The transition multipole, $\ell_{\rm hybrid}$ is marked by dotted vertical lines.

(A color version of this figure is available in the online journal.)

symmetrized transfer function directly in harmonic space for one of the V1 simulations. Thus, the two convolved maps have identical power spectra but slightly different phases. The top panel shows the full-sky difference map with a temperature scale of ± 5 μK. The lower panels show two selected $15^\circ \times 15^\circ$ regions centered on the north ecliptic pole (NEP; top row) and the Galactic center (GC; bottom row), respectively. The left column shows the actual temperature map convolved with the asymmetric beam, and the right column shows the same differences as in the full-sky plot.

The first striking feature seen in this map is that the differences are clearly larger in the ecliptic plane than around the ecliptic poles. This is due to the *WMAP* scanning strategy, which leads to a larger number of observations per pixels around the poles, and also with a greater range of beam orientations. Next, it is difficult to spot any single unambiguous and well-defined correlation between the convolved and the difference maps. Clearly, there are similar morphological structures in the two, but the sign of the correlations appears to vary. Third, we see a clear tendency of diagonal striping in the GC plot,

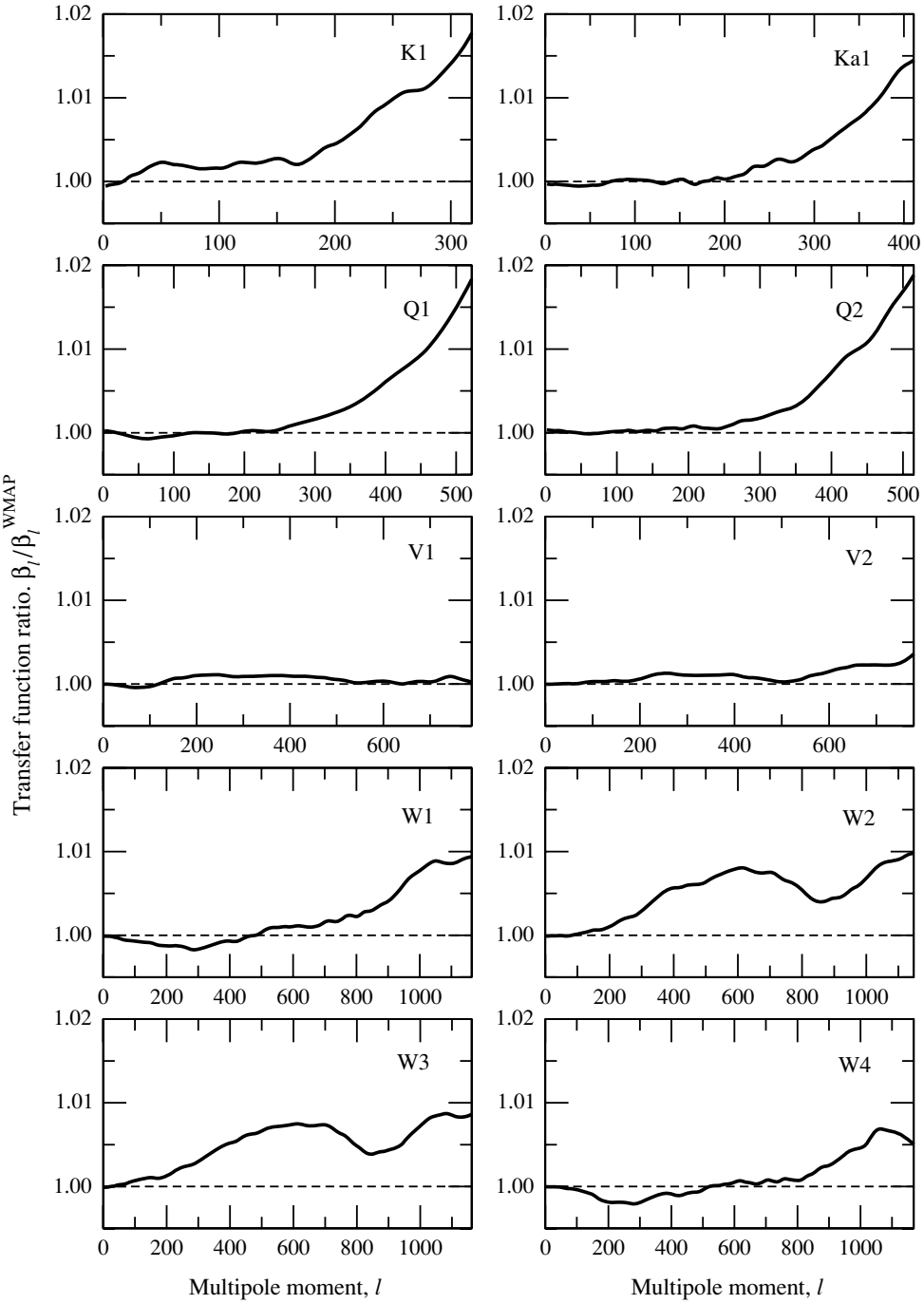

Figure 4. Ratio between the transfer functions derived in this paper and the nominal *WMAP* transfer functions for all DAs. Note that the DAs split into two main groups depending on the focal plane position: the outer DAs, K1, Ka1, and Q1–2, all rise with ℓ, whereas the inner DAs, V1–2 and W1–4, decrease with ℓ. Note also the similarity between W1 and W4, between W2 and W3, and between V1 and V2.

which corresponds to correlations along ecliptic meridians and lines of constant latitude (note that these plots are shown in Galactic coordinates, while the *WMAP* scanning strategy is nearly azimuthally symmetric in ecliptic coordinates).

In the following section, we consider the impact of the asymmetric beams on cosmological parameters. However, before concluding this section we make a comment concerning an outstanding issue regarding the 3-year *WMAP* power spectra first noted by Eriksen et al. (2007). They pointed out the presence of a 3σ amplitude discrepancy between the *V*- and *W*-band power spectra (Figure 5 of Eriksen et al. 2007). Specifically, the *V*-band spectrum was biased low compared to the *W*-band spectrum between $\ell = 300$ and 600 by $\sim 80\ \mu\mathrm{K}^2$. Huffenberger et al. (2006) later showed that $\sim 30\ \mu\mathrm{K}^2$ of this discrepancy could be attributed to overestimation of point source power in the 3-year *WMAP* spectrum analysis, and this was subsequently confirmed and corrected by Hinshaw et al. (2007). Still, about $50\ \mu\mathrm{K}^2$ of this difference remained, which was statistically significant at $\sim 2\sigma$.

Eriksen et al. (2007) proposed that this difference might be due to errors in the beam transfer functions caused by asymmetric beams. Given the new results presented in this paper, we are now in a position to consider this issue more quantitatively. The relevant question is then whether the *WMAP V*-band

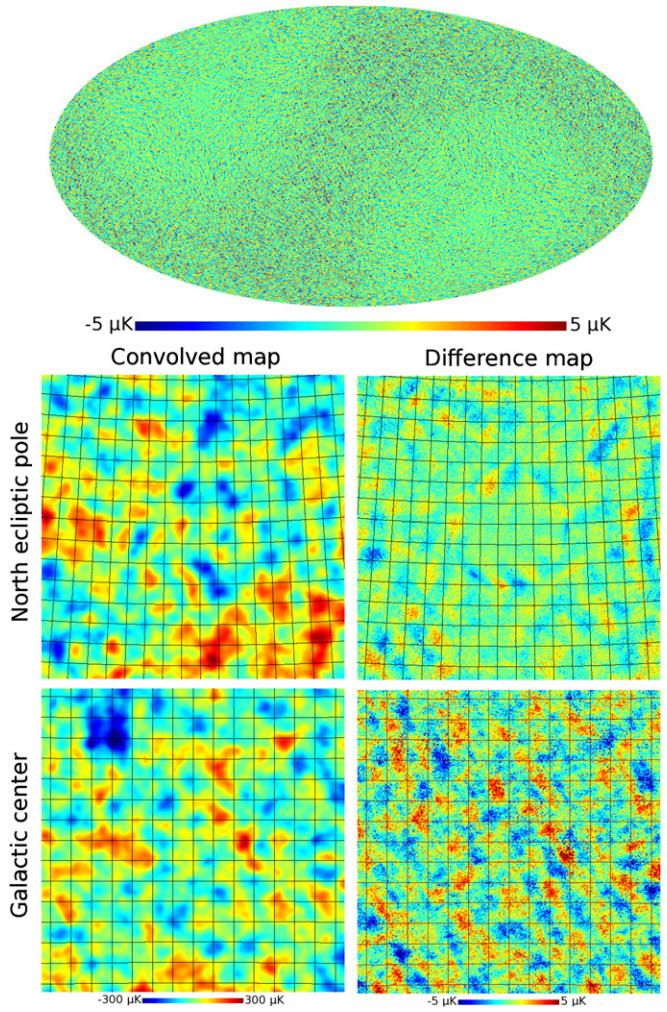

Figure 5. Top panel: difference between a V1 simulation convolved with the full asymmetric beam and the same realization convolved with the corresponding symmetrized transfer function. The two maps have identical power spectrum but different phases. Note that larger differences are observed along the ecliptic plane, where the density of observations is lower than toward the ecliptic poles, and the cross-linking is also weaker. Bottom panels: zoom-in on two regions, the north ecliptic pole (NEP; top row) and the Galactic center (GC; bottom row). Left column shows the map convolved with an asymmetric beam, and right column shows the same difference as in the top panel.

transfer functions are systematically biased high compared to the *W*-band functions. At first glance, one may get this impression from the plots shown in Figure 4. The *V*-band ratios are both very close to unity over the full range, whereas W2 and W3 are slightly high in the same range, at about 0.5%. On the other hand, W1 and W4 are also very close to zero in the same range. The net difference is therefore not more than a few tenths of a percent, which corresponds to $\sim 10\ \mu\mathrm{K}^2$ in the power spectrum. Thus, it is possible that this effect may contribute somewhat to the power spectrum discrepancy between *V* and *W* bands, but it does not seem to fully explain the difference.

6. IMPACT ON COSMOLOGICAL PARAMETERS

For completeness, we now assess the impact of asymmetric beams in *WMAP* on cosmological parameters. We do this by modifying the co-added 5-year *WMAP* temperature power spectrum (Nolta et al. 2009) provided with the *WMAP* likelihood code (Dunkley et al. 2009; Komatsu et al. 2009) according to the transfer function ratios shown in Figure 4, and run CosmoMC (Lewis & Bridle 2002) to estimate the resulting parameters. Only a simple six-parameter ΛCDM model is considered in this paper. For comparison, we also run the code with the nominal *WMAP* spectrum as input, so that we can directly estimate the impact of asymmetric beams with everything else held fixed.

Unfortunately, the individual cross-spectra for each pair of DAs have not yet been published by the *WMAP* team, but only the total co-added spectrum. We must therefore make a few approximations in order to apply the proper beam corrections to the full spectrum. First, let σ_n^i denote the white noise level of DA i (see Table 1), β_ℓ^i the transfer function estimate derived in this paper, and let $\beta_\ell^{i,WMAP}$ be the nominal *WMAP* transfer function. Finally, define

$$\delta_\ell^i = \frac{\beta_\ell^i}{\beta_\ell^{i,WMAP}} - 1 \tag{13}$$

to be the fractional difference between the two.

Next, the *WMAP* team uses the MASTER pseudo-spectrum algorithm (Hivon et al. 2002) for power spectrum estimation (Hinshaw et al. 2003, 2007; Nolta et al. 2009), which quickly produces good estimates at high ℓ's. However, this method is not a maximum-likelihood estimator, and it does not yield optimal error bars. To improve on this, the *WMAP* applies different pixel weights in different multipole regions: at low ℓ's, where the sky maps are signal dominated, they apply equal weights to all pixels, while at high ℓ's, where the maps are noise dominated, they apply inverse noise variance pixels weights. These weights are then taken into account when co-adding the cross-spectra obtained from all possible DA pairs (but excluding auto-correlations). The transition is made at $\ell = 500$.

The beam-convolved (but noiseless) power spectrum $\tilde{C}_\ell^{ij}$ observed by a given DA pair, i and j, may be written as $\tilde{C}_\ell^{ij} = \beta_\ell^i \beta_\ell^j C_\ell$, where C_ℓ is the true power spectrum of our sky, and β_ℓ^i is the true transfer function for DA i. The noise amplitude of the same spectrum is proportional to $\sigma_n^i \sigma_n^j / \beta_\ell^i \beta_\ell^j$. The inverse noise variance weight of this cross-spectrum is therefore approximately

$$w_{ij} = \frac{\frac{\beta_\ell^i \beta_\ell^j}{\sigma_n^i \sigma_n^j}}{\sum_{i'<j'} \frac{\beta_\ell^{i'} \beta_\ell^{j'}}{\sigma_n^{i'} \sigma_n^{j'}}}, \tag{14}$$

where the sum runs over all N different pairs of cross-spectra. Note that this is only an approximation to the exact expression, because other effects also enter the full calculations. One important example is the sky cut, which couples different ℓ modes, and is taken into account through a coupling matrix. Such effects are not included in the analysis presented here.

Pulling all of this together, the appropriately co-added power spectrum provided by *WMAP* should ideally read

$$\hat{C}_\ell = \begin{cases} \frac{1}{N} \sum_{i<j} \frac{\tilde{C}_\ell^{ij}}{\beta_\ell^i \beta_\ell^j} & \text{for} \quad \ell \leqslant 500 \\ \sum_{i<j} w_{ij} \frac{\tilde{C}_\ell^{ij}}{\beta_\ell^i \beta_\ell^j} & \text{for} \quad \ell > 500 \end{cases}. \tag{15}$$

However, the spectrum that in fact is provided by *WMAP* is Equation (15), evaluated for $\beta_\ell = \beta_\ell^{WMAP}$, which, according to our calculations, is slightly biased. To obtain the appropriate correction factor, $\alpha_\ell = \hat{C}_\ell / \hat{C}_\ell^{WMAP}$, for each ℓ, we therefore set

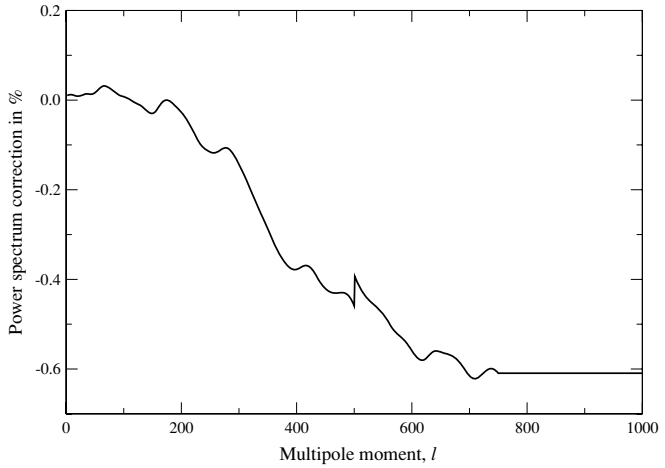

Figure 6. Total correction to the 5-year co-added *WMAP* temperature power spectrum due to asymmetric beams. Note the transition between high and low signal-to-noise weighting schemes at $\ell = 500$, and also the manually capped amplitude at $\ell > 750$. The latter is imposed in order to be conservative in the very high-ℓ regime, where the transfer functions are sensitive to pixel window effects.

$\beta_\ell = \beta_\ell^{WMAP}(1 + \delta_\ell)$ in Equation (15) and expand to first order in δ_ℓ. Doing this, we find that

$$\alpha_\ell = \begin{cases} 1 - \frac{1}{N}\sum_{i<j}\left(\delta_\ell^i + \delta_\ell^j\right) & \text{for} \quad \ell \leqslant 500 \\ 1 - \sum_{i<j} w_{ij}^{WMAP}\left(\delta_\ell^i + \delta_\ell^j\right) & \text{for} \quad \ell > 500, \end{cases} \tag{16}$$

where w_{ij}^{WMAP} is the expression given in Equation (14) evaluated with β_ℓ^{WMAP}.

This function is plotted in Figure 6. Note, however, that we have capped the function by hand at $\ell = 750$ to be conservative, considering that our *V*-band transfer functions do not have support all the way to the maximum multipole used in the *WMAP* likelihood code, $\ell_{\rm max} = 1000$.

The results from the corresponding CosmoMC analyses are tabulated in Table 2 in terms of marginal means and standard deviations. Here we see that there are only very small shifts in the resulting parameters, indicating good stability with respect to beam asymmetries in *WMAP*. For example, there is a negative shift of -0.2σ in the amplitude of scalar perturbations, $A_{\rm s}$, and -0.1σ in the spectral index of scalar perturbations.

7. CONCLUSIONS

This paper has two main goals. First, we wanted to generate a set of *WMAP*-like simulations that fully take into account the asymmetric beams and anisotropic scanning pattern of the *WMAP* satellite. Such simulations are extremely valuable for understanding the impact of beam asymmetries on various statistical estimators and models. One example of such, which indeed provided us with the initial motivation for studying this issue, is the anisotropic universe model presented by Ackerman et al. (2007), and later considered in detail with respect to the *WMAP* data by Groeneboom & Eriksen (2009). The result from that analysis was a tentative detection of violation of rotational invariance in the early universe, or some other effect with similar observational signatures, at the 3.8σ confidence level. It was shown that neither foregrounds nor correlated noise could have generated this signal, but the question of asymmetric beams was left unanswered. This issue will be revisited in an upcoming paper, using the simulations generated here.

Table 2
Cosmological Parameters

Parameter	Nominal *WMAP*	Corrected Beams	Shift in σ
$\Omega_{\rm b}h^2$	0.0228 ± 0.0006	0.0228 ± 0.0006	0.0
$\Omega_{\rm cdm}h^2$	0.109 ± 0.0006	0.109 ± 0.006	0.0
$\log(10^{10}A_{\rm s})$	3.064 ± 0.042	3.058 ± 0.042	-0.2
τ	0.089 ± 0.017	0.089 ± 0.017	0.0
h	0.722 ± 0.027	0.725 ± 0.026	0.1
$n_{\rm s}$	0.965 ± 0.014	0.964 ± 0.014	-0.1

Notes. Comparison of cosmological parameters derived from the nominal *WMAP* power spectrum (second column) and from the power spectrum corrected for asymmetric beams (third column). The rightmost column shows the relative shift between the two in units of σ.

The second goal of the paper was to assess the impact of beam asymmetries on the *WMAP* power spectrum and cosmological parameters. We did this by comparing the power spectrum of the full beam convolved simulations with the power spectrum of the input realizations, thereby providing a direct estimate of the effective beam transfer functions. Doing so, we found differences at the 0.5% level in several DAs at intermediate and high ℓ's with respect to the nominal *WMAP* transfer functions.

A similar analysis was performed for the 3-year *WMAP* data release by Hinshaw et al. (2007), who approach the problem from an analytical point of view. However, at that time only the A-side beams were available (Hill et al. 2009), and they therefore assumed identical beams on both the A and B sides. With these data, they concluded that the impact of beam asymmetries was $\lesssim$1% everywhere below $\ell = 1000$ for the *V*- and *W*-band DAs, in good agreement with our findings.

As far as cosmological parameters go, the impact of asymmetric beams is small. Specifically, we find shifts of -0.2σ in the amplitude of scalar perturbations, $A_{\rm s}$, and -0.1σ in the spectral index of scalar perturbations, $n_{\rm s}$.

The simulations described in this paper may be downloaded from I.K.W.'s Web site.[8]

The authors thank Ned Wright for very useful and stimulating discussions, which eventually led to the conception of this project, and the referee for very useful comments. We also thank Kris Górski, Sanjit Gupta, Gary Hinshaw, and Graca Rocha for interesting discussions, and the *WMAP* team for providing the required data for the project, including the beam pixel window function. L.A. thanks the Institute of Theoretical Astrophysics, Oslo, for its generous hospitality during her visit to Norway. I.K.W., H.K.E., and N.E.G. acknowledge financial support from the Research Council of Norway. The computations presented in this paper were carried out on Titan, a cluster owned and maintained by the University of Oslo and NOTUR. Some of the results in this paper have been derived using the HEALPix (Górski et al. 2005) software and analysis package. We acknowledge use of the Legacy Archive for Microwave Background Data Analysis (LAMBDA). Support for LAMBDA is provided by the NASA Office of Space Science.

APPENDIX A

CONVERGENCE OF THE DIFFERENTIAL MAP MAKER

As described in Section 2.2, we introduce one new step to the differential map making algorithm presented by Wright

[8] http://www.fys.uio.no/~ingunnkw/WMAP5_beams

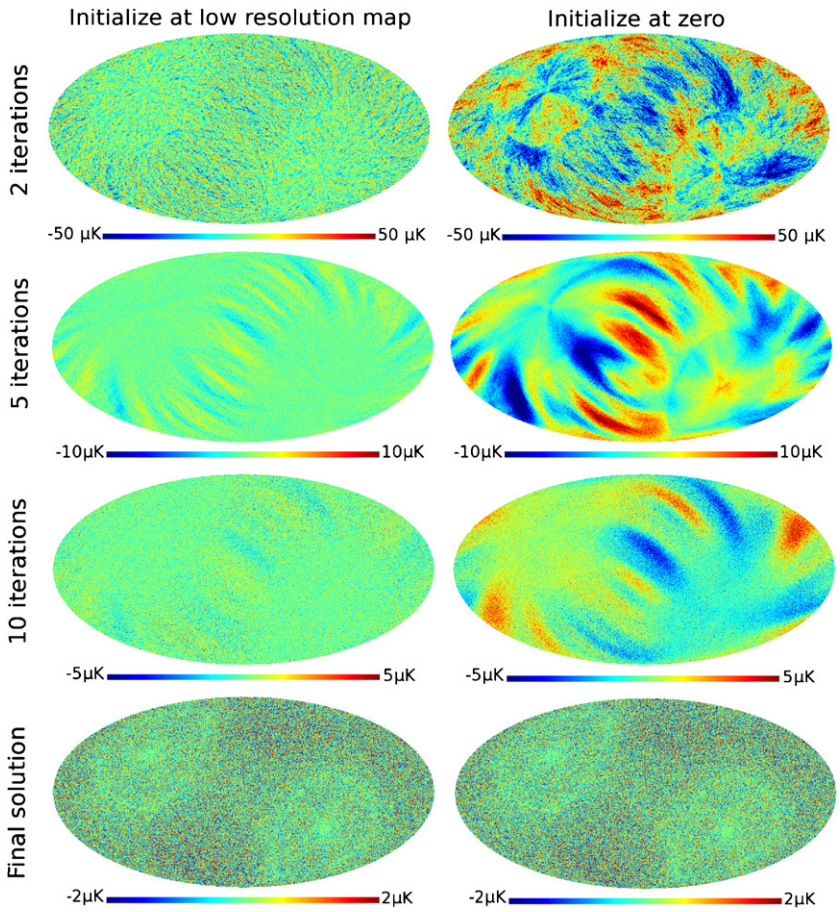

Figure 7. Comparison of convergence of the differential map maker for two different choices of initialization. The left column shows the snapshots from the series obtained with initializing at a solution obtained by brute-force evaluation at low resolution, while the right column shows the series obtained when initializating at zero. Each plot is a difference map between the current solution for a data set including asymmetric beams and real scanning strategy and the corresponding map convolved with the analytic Gaussian beam and isotropic HEALPix pixel window. The bottom row shows the final solutions obtained in the two cases, which were obtained after 67 and 123 iterations, respectively. These final maps are idential up to a $\sim$0.1 μK dipole.

et al. (1996): we initialize the iterations at the exact solution of Equation (7) evaluated at low resolution, which in this paper is taken to be $N_{\rm side} = 16$, with 3072 pixels.

To demonstrate the improvement in convergence due to this choice of initialization, we revisit the analytic case considered in Section 4, which compared the results from our simulation pipeline with an exact analytic case, but taking into account the actual *WMAP* scanning strategy.

In Figure 7, we show a set of difference maps taken between the intermediate solutions produced by the differential map maker and the analytic and isotropic map solutions. From top to bottom, the panels show the residuals after 2, 5, and 10 iterations, and at the bottom, the final converged solutions. The left panel shows the series obtained when initializing the search at the low-resolution solution, while the right panel shows the series when initializing at zero. Convergence was achieved respectively after 67 and 123 iterations in the two cases.

Note that the *WMAP* team initializes their search at the CMB dipole, which is the dominant component in their data set. However, this is in our setting equivalent to initializing at zero, since our simulation does not include a dipole.

Taking the difference between the two final solutions, we have verified that the peak-to-peak residuals in the two maps are less than 0.1 μK, of which essentially all is concentrated in a single dipole component. The solution is thus independent of initialization, and the only difference lies in computational speed.

Finally, note that even though the two maps are internally indistinguishable, they are both quite different from the isotropic reference map. To be precise, the rms difference between the derived maps and the isotropic reference map is 0.91 μK, with a spatial pattern similar to the overall *WMAP* scanning pattern.

The cause of these residuals is the differences in the treatment of the effective pixel windows: the HEALPix pixel window is computed by uniformly averaging over the full sky, whereas the simulation pipeline takes into account the actual pointing directions of the satellite. Sub-pixel variations in the CMB sky therefore lead to significant differences in the two estimates on small scales. The effect of such pixel window variations on the 5-year *WMAP* power spectrum will be considered in a future paper.

APPENDIX B

FAST TWO-DIMENSIONAL SPLINE EVALUATION

The heart of the simulation pipeline described in Section 2 is the real-space convolution algorithm defined by Equation (4). For this operation to be computationally feasible we have to be able to evaluate the beam response function quickly at any position. The real beam maps, however, are provided to us in the form of two-dimensional pixelized images with relatively coarse resolution. It is therefore necessary to establish a fast and accurate interpolation scheme.

We adopt a bicubic spline for this purpose and review here one specific implementation of this concept. Note that most of the following is standard textbook material (e.g., Press 2002), and is included here only for easy reference.

Suppose we are given some tabulated two-dimensional function $f(x, y)$ over a regular grid, and want to interpolate at arbitrary positions (x_0, y_0) within this grid. One particularly appealing approach for doing so is by means of bicubic splines, which are bi-cubic polynomials in x and y,

$$p(x, y) = \sum_{i=0}^{3} \sum_{j=0}^{3} a_{ij} x^i y^j. \tag{B1}$$

The coefficients a_{ij} are defined separately for each grid cell, and our task is to compute these given the tabulated function $f(x, y)$. Note that once we have these coefficients, any spline evaluation will be very fast, since it essentially amounts to performing a vector–matrix–vector multiplication with a 4×4 matrix.

Let us first consider a cell defined over the unit square, having corners $(x, y) = (0, 0)$, $(1, 0)$, $(0, 1)$, and $(1, 1)$ (note that this assumption does not imply any restriction of the problem, since any grid cell in a regular grid may be linearly transformed into the unit square). Assume also that we know the function values $f(x, y)$ and the first- and second-order derivatives, $f_x(x, y)$, $f_y(x, y)$, and $f_{xy}(x, y)$ at all four corners (here subscript x denotes derivatives, $f_x = df/dx$). The coefficients of the bicubic spline are then defined such that both the function values and the derivatives match,

$$f(x, y) = p(x, y) \tag{B2}$$

$$f_x(x, y) = p_x(x, y) \tag{B3}$$

$$f_y(x, y) = p_y(x, y) \tag{B4}$$

$$f_{xy}(x, y) = p_{xy}(x, y), \tag{B5}$$

at all four corners. With four equations for each of four corners, there is a total of 16 independent equations for the 16 independent spline coefficients, a_{ij}, and the spline is therefore uniquely defined.

Writing out Equation (B5) explicitly, we obtain the following set of linear equations:

$$\left.\begin{aligned} f(0, 0) &= p(0, 0) = a_{00} \\ f(1, 0) &= p(1, 0) = a_{00} + a_{10} + a_{20} + a_{30} \\ f(0, 1) &= p(0, 1) = a_{00} + a_{01} + a_{02} + a_{03} \\ f(1, 1) &= p(1, 1) = \textstyle\sum_{i=0}^{3} \sum_{j=0}^{3} a_{ij} \end{aligned}\right\} \tag{B6}$$

$$\left.\begin{aligned} f_x(0, 0) &= p_x(0, 0) = a_{10} \\ f_x(1, 0) &= p_x(1, 0) = a_{10} + 2a_{20} + 3a_{30} \\ f_x(0, 1) &= p_x(0, 1) = a_{10} + a_{11} + a_{12} + a_{13} \\ f_x(1, 1) &= p_x(1, 1) = \textstyle\sum_{i=0}^{3} \sum_{j=0}^{3} i\, a_{ij} \end{aligned}\right\} \tag{B7}$$

$$\left.\begin{aligned} f_y(0, 0) &= p_y(0, 0) = a_{01} \\ f_y(1, 0) &= p_y(1, 0) = a_{01} + a_{11} + a_{21} + a_{31} \\ f_y(0, 1) &= p_y(0, 1) = a_{01} + 2a_{02} + 3a_{03} \\ f_y(1, 1) &= p_y(1, 1) = \textstyle\sum_{i=0}^{3} \sum_{j=0}^{3} j\, a_{ij} \end{aligned}\right\} \tag{B8}$$

$$\left.\begin{aligned} f_{xy}(0, 0) &= p_{xy}(0, 0) = a_{11} \\ f_{xy}(1, 0) &= p_{xy}(1, 0) = a_{11} + 2a_{21} + 3a_{31} \\ f_{xy}(0, 1) &= p_{xy}(0, 1) = a_{11} + 2a_{12} + 3a_{13} \\ f_{xy}(1, 1) &= p_{xy}(1, 1) = \textstyle\sum_{i=0}^{3} \sum_{j=0}^{3} ij\, a_{ij} \end{aligned}\right\}. \tag{B9}$$

Equations (B6)–(B9) represent the matching function values, the first-order x- and y-direction derivatives, and the second-order x/y cross derivatives, respectively.

The remaining problem is then to estimate the first- and second-order derivatives at all grid points, and several approaches may be used for this. We adopt a spline-based method for this step as well.

First, we compute a standard one-dimensional natural spline along all x and y coordinate lines, using standard methods. The result from this operation is the set of all pure second-order derivatives, $f_{xx}(x, y)$ and $f_{yy}(x, y)$, at each grid point.

Because a one-dimensional spline is also a simple cubic polynomial, and therefore only has four free coefficients, it is sufficient to know the function values and second-order derivatives at all grid corners to uniquely specify every coefficient. As a consequence of this, the first-order derivative along the x-direction at grid point (x_i, y_j) is uniquely given by Press (2002),

$$f_x(x_i, y_j) = \frac{f(x_{i+1}, y_j) - f(x_i, y_j)}{h_x} - \frac{1}{3} h_x f_{xx}(x_i, y_j). \tag{B10}$$

Here $h_x = x_{i+1} - x_i$ is the x-direction grid cell size for the current cell. An equivalent expression obviously holds for the y-direction derivatives.

Finally, to estimate the second-order cross-derivatives, $f_{xy}(x, y)$, the above process is repeated such that y-derivatives are computed from $f_x(x, y)$ splines for all y-direction coordinate lines. Thus, all required derivatives may be obtained by performing $m + 2n$ one-dimensional spline computations, where m is the number of grid cells in the x-direction, and n is the number of grid cells in the y-direction.

REFERENCES

Ackerman, L., Carroll, S. M., & Wise, M. B. 2007, Phys. Rev. D, 75, 083502
Bennett, C. L., et al. 2003, ApJS, 148, 1
Dunkley, J., et al. 2009, ApJS, 180, 306
Eriksen, H. K., et al. 2007, ApJ, 656, 641
Górski, K. M., Hivon, E., Banday, A. J., Wandelt, B. D., Hansen, F. K., Reinecke, M., & Bartelman, M. 2005, ApJ, 622, 759
Green, P. J., & Silverman, B. W. 1994, Nonparametric Regression and Generalized Linear Models (London: Chapman and Hall)
Groeneboom, N. E., & Eriksen, H. K. 2009, ApJ, 690, 1807
Groeneboom, N. E., Eriksen, H. K., Górski, K., Huey, G., Jewell, J., & Wandelt, B. 2009, ApJ, 702, L87
Hill, R. S., et al. 2009, ApJS, 180, 246
Hinshaw, G., et al. 2003, ApJS, 148, 63
Hinshaw, G., et al. 2007, ApJS, 170, 288
Hinshaw, G., et al. 2009, ApJS, 180, 225
Hivon, E., Górski, K. M., Netterfield, C. B., Crill, B. P., Prunet, S., & Hansen, F. 2002, ApJ, 567, 2
Huffenberger, K. M., Eriksen, H. K., & Hansen, F. K. 2006, ApJ, 651, L81
Jarosik, N., et al. 2007, ApJS, 170, 263
Komatsu, E., et al. 2009, ApJS, 180, 330
Lewis, A., & Bridle, S. 2002, Phys. Rev. D, 66, 103511
Nolta, M. R., et al. 2009, ApJS, 180, 296
Page, L., et al. 2003, ApJS, 148, 39
Press, W. H. 2002, Numerical Recipes in C++: The Art of Scientific Computing (Cambridge: Cambridge Univ. Press)
Wandelt, B. D., & Górski, K. M. 2001, Phys. Rev. D, 63, 123002
Wright, E. L., Hinshaw, G., & Bennett, C. L. 1996, ApJ, 458, L53